The Ninth International Conference on Modeling and Diagnostics in Engine Systems (COMODIA 2017), July 25-28, 2017, Okayama, Japan
SAND2017-6747C

C103

Time-resolved Measurements of Mixing Quantities in Diesel Jets

Julien Manin[1,2,*], Lyle M. Pickett[1], Scott A. Skeen[1], Jonathan H. Frank[1]

[1]*Sandia National Laboratories, 7011 East Ave, Livermore CA, USA*
[2]*Artium Technologies, 470 Lakeside Dr., Sunnyvale CA, USA*
**Corresponding author: Julien Manin (jmanin@artium.com)*

Key Words: Diesel sprays, Mixing measurements, Rayleigh scattering, Scalar dissipation, Turbulent length scales

ABSTRACT

Fuel and oxidizer mixing is a key parameter influencing combustion and emission performance in diesel engines. At the same time, quantitative mixing measurements in automotive sprays are very challenging such that only a few experimental results are available as targets for the development and tuning of numerical models. The caveat is that the experimental data mainly concern the quasi-steady part of the jet, while it can be argued that the injection process in current alternative thermal engines is mostly transient. This work applies planar laser Rayleigh scattering at high-frequency to resolve the development and mixing of vaporized diesel sprays injected in a highly-pressurized environment. The state-of-the-art equipment employed for these experiments include a purposely-built high-power, high-repetition rate pulsed burst laser, optimized optics and a state-of-the-art high-speed CMOS camera. Advanced image processing methods were developed and implemented to mitigate the negative effects of the extreme environments found in diesel engines at the time of injection. The experiments provided two-dimensional mean and variance of the mixture and temperature quantities. The optical system's high spatial and temporal resolution enables tracking of the mixing field with time and space, from which temporally and spatially correlated mixing quantities can be extracted. Further analysis of the detailed mixture and temperature fields offered information about the turbulent mixing process of high-pressure diesel sprays such as scalar dissipation rates or turbulent length scales. Substantial effort was made to assess the uncertainties and limitations of such experimental results due to the optically challenging environment.

INTRODUCTION

With the increasingly stringent emission regulations and fuel efficiency requirements set by both the governments and the consumers, the thermal engine must make substantial progress to propel vehicles for decades to come. Passenger cars or light-duty vehicles have improved such that this sector's fuel demand is declining. This trend has yet to be seen for heavy-duty vehicles, for which forecasts predict a rise in fuel demand over the next decades. Heavy-duty transportation mainly relies on diesel engines as a power source because they are more efficient than their gasoline counterpart; however, diesel engines have been criticized for their higher pollutant emissions. The mixing process between the injected fuel and the oxidizer in diesel engines has been recognized as a key parameter for clean and efficient diesel combustion. Highly detailed quantitative measurements are needed to fully understand the physics of spray vaporization and mixing, which will enable the development of high-fidelity models. Such models will provide engine manufacturers with a cost-effective means for the design of high-efficiency, low-emission engines capable of achieving mandated targets.

Experimental studies have been performed on mixing in diesel engines, but the relative complexity induced by the high pressures and temperatures inside the combustion chamber make such measurements difficult [1]. Many approaches have been implemented, some diagnostics providing single-point or 1-D line [2] measurements, while others provided a more global picture, with 2-D planar [3, 4] or path-integrated mixing distributions [5]. These techniques have been very useful to leverage the global understanding of spray mixing at one point in time or another. Two-dimensional techniques have generally been preferred as they deliver spatial variation across the mixing field. The major criticism has been that these techniques have only been applied to deliver single-shot results of the mixing field, as opposed to time-resolved data. Only the recent advances in equipment have made it possible to apply the different diagnostics at high-speed, with examples of planar laser-induced fluorescence (PLIF) experiments in gaseous jets by several groups as detailed by Sick [6].

PLIF has been one of the most widely applied diagnostics in combustion research, and is often considered in spray

systems because the inelastic nature of the signal (wavelength shift) can be discriminated from elastic Mie scatter from droplets. The PLIF technique can be applied at high speed, provided a high-speed laser exciting the fluorophore (tracer) at the appropriate wavelength is available, along with a high-speed camera. The major issue with PLIF when aiming at quantifying fuel concentration in vaporizing sprays is the calibration. Most tracers are sensitive to temperature, requiring careful calibration of the tracer as function of temperature (under the relevant pressure condition for completeness). Because of the lower temperature of the injected fluid compared to the ambient under vaporizing conditions, the mixing of the two fluids induce temperature gradients, which may not be easily assessed. Another drawback of PLIF, affecting most laser measurements, is the dependence upon laser intensity distribution. The fluorescence signal is expected to be proportional to the incoming laser intensity. Under high temperature and pressure conditions, such as those in diesel engines, the intensity distribution may be strongly affected by the refractive index gradient inside the chamber. These spatial variations in refractive index coming from gradients in density result in beam steering, making it difficult to estimate the spatial laser intensity distribution in the measurement region.

Another attractive technique for planar measurement of mixing and/or temperature is Rayleigh scattering. Applied in evaporative sprays by Espey et al. [7], planar laser Rayleigh scattering (PLRS) provides a direct measure of the molecule number density of the species or mixture. Unlike PLIF, PLRS is an elastic light scattering technique, meaning that the radiated wavelength is equal to the incoming illumination. As such, the Rayleigh signal of interest is easily overwhelmed by reflections and other scattering interference, which may result in a relatively high background flare or noise. The elastic light interference is often considered as the main difficulty when applying quantitative Rayleigh scattering. The high-pressure environments in diesel engine reduces the impact of background flare because of the increase in molecular number density. On the other hand, the spatial coexistence of liquid droplets and vaporized fuel represent yet another challenge for Rayleigh scattering under these conditions. But researchers [3, 7, 8, 9], including our group, have overcome these challenges by addressing these problems systematically.

As mentioned earlier, time-resolved data of the mixing field in diesel sprays under relevant conditions are lacking. The experience acquired by the authors through the several experimental campaigns on mixing measurements using PLRS represent a strong argument for applying the technique at high-speed. To this end, advanced high-speed laser and imaging systems were developed by our group. The experiments were treated not only to deliver time-resolved quantitative mixing fields, but to also explore the potential to extract detailed mixing quantities such as scalar dissipation rates or turbulent length scales. To the authors' knowledge, such quantities have never been published for evaporative diesel jets. This manuscript is organized in five sections, including the present introduction. The following section details the experimental setup, with the necessary information regarding the high-speed, high-power pulsed burst laser and imaging system. The high-temperature, high-pressure optically-accessible spray vessel is also presented in the second section, along with the injection system and conditions. The image processing methods and mathematics to obtain quantitative mixing information from the images are described in the third section. The fourth section presents and discusses the mixing results. The fifth and final section concludes this manuscript.

EXPERIMENTAL SETUP

High-speed Rayleigh scatter imaging system

As mentioned in the introduction, a key element of the Rayleigh scattering diagnostic implemented in this work is the high-speed, high-power pulsed burst laser developed by the authors. The laser system was designed to provide pulse energies sufficient for Rayleigh scattering measurements at repetition rates adequate for the high flow velocities encountered in high-pressure sprays. The system can deliver these high-frequency, high-energy pulses of short durations (below 10 ns), over a burst duration of 5 ms or 500 pulses [10].

To measure the Rayleigh scattered signal over an area relevant to global diesel jet mixing, the laser was expanded to form a 20-mm wide collimated sheet. The output of the second harmonic generator was relay imaged onto the input of the sheet-forming optics, in order to limit diffraction. The laser was expanded and collimated by a set of cylindrical lenses, while a 500-mm cylindrical lens focused the beam to achieve a thin laser sheet (approximately 130 μm) within the measurement volume. At the measurement location, the laser sheet covered a region from about 15 mm to 35 mm downstream of the injector exit, crossing at the spray centerline.

Maps of the Rayleigh scattered signal were acquired by a commercial high-speed camera (Photron SA-X2). The camera was equipped with a Nikkor Noct 58 mm, f/1.2 lens, to which a 2-diopter doublet close-up lens was attached. The projected pixel size of the system in this configuration was 78 μm/pix. The camera was synchronized with the laser, for an operating frequency of 100 kHz. At this framerate, the digital detector field was 384 x 264 pix^2. The electronic shutter time was set to 2.5 μs, but was ultimately defined by the laser pulse duration. A 532-nm interference filter was placed in front of the close-up lens to eliminate interfering signal from external lighting or other visible or near-IR emissions.

Imaging setup performance

The optical performance of the imaging system is important when quantifying spatial scales. This consideration becomes especially critical when the object plane is immersed in environments where distortion may occur—such as in this study where the high pressure and temperature in the chamber exacerbates beam steering. The response of the imaging system has been measured

under the thermodynamic conditions in the chamber simulated during the experiments, i.e. 900 K temperature and 6.0 MPa pressure. The knife-edge technique was used to evaluate the response of the imging system to a sharp-edge. The object plane was illuminated by a collimated light source, at a wavelength similar to that of the laser radiation used in the experiments, and providing about half the digital intensity scale of the camera (similar in intensity to the Rayleigh signal in the experiments). A sharp edge was placed at the object plane and images were acquired during simulated thermodynamic conditions. The response of the system to the sharp edge, called the edge spread function, can be used to extract the line spread function by spatial derivative of the edge response.

Spatial filtering is commonly applied to images to reduce noise, which is known to affect the quantification of mixing parameters on a single-shot basis. The least amount of filtering is desirable due to the spatial resolution degradation introduced by spatial filtering. Gaussian-shaped spatial filters are generally preferred to mean filters because of the intensity profile weighted toward the central pixels of the kernel, thus resulting in a smoother transition at the edges of the filter box. Two filtering levels have been tested on the images, with characteristic dimensions of three and five pixels. The filters use square-shaped kernels (3 x 3 or 5 x 5), and are applied uniformly across the images.

Figure 1 plots the normalized edge and line spread functions, with the distance from the edge represented in abscissa. The curves report the response of the imaging system for the unfiltered original images, as well as for the two spatial filtering levels of three and five pixels characteristic dimensions.

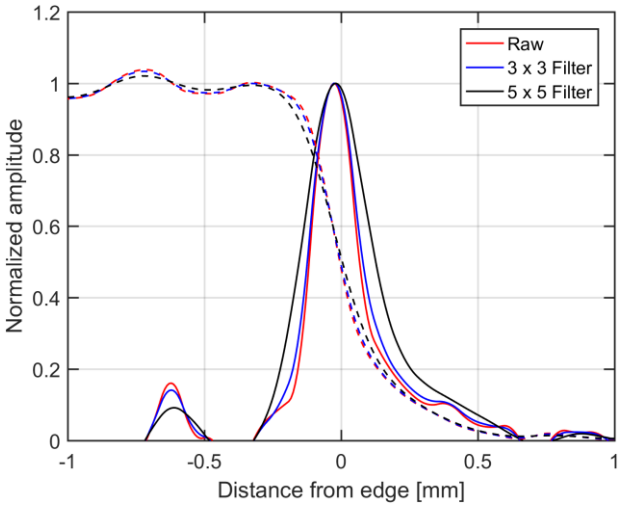

Fig. 1 Edge (dashed lines) and line (solid lines) spread functions measured by the imaging system under the experimental conditions. The plot compares the response of the original image to spatially filtered maps with two filter stencils dimensions.

The tests aiming at characterizing the spatial response of the imaging system reported in Fig. 1 reveal a line spread function of 183 μm evaluated at full-width at half-maximum for the unfiltered images. No measurable difference was observed when evaluating the line spread function at several locations within the visualized field. Applying Gaussian filtering degraded the spatial resolution of the rendered images, with profiles spreading over 204 and 281 μm with filter stencil dimensions of three and five pixels, respectively. These results mean that even when no filter is applied, the image-based resolution of the system spreads over two pixels. The final resolution of the system determines the dimension of the spatial features that can be quantified. Spatial dimensions near the measured resolution of the system, for the respective filtering level, cannot be ascertained due to the possible blur. The mixing length scales presented in the results section should be analyzed and quantified accounting for the actual resolution of the images.

The depth of field also affects the spatial response of the imaging system, due to the integration of the signal in the third (out-of-plane) dimension. The camera and lens system have been observed to provide a narrow depth of field, but the depth of the image is ultimately controlled by the thickness of the laser sheet. Based on the optics and input beam characteristics, the laser sheet thickness is expected to be approximately 130 μm thick at the waist, as calculated using the Gaussian beam equation. The sheet should remain thin throughout the visualized region thanks to the small initial beam diameter and relatively long focal length of the 500-mm focusing cylindrical lens. The signal scattered by the molecules and collected by the camera system is integrated over the laser sheet thickness, meaning that the integrated signal thickness is smaller than the effective resolution in the object plane. Kaiser and Frank [11] investigated the impact of laser sheet thickness on mixing measurements and found that the effect of out-of-plane integration on in-plane spatial structures was minor and could be neglected. It should also be noted that the out-of-focus blur produced by a 130-μm offset from the focal plane is not anticipated to negatively impact spatial resolution of the system discussed above.

Spray vessel and injection system

A single-hole research injector was used to inject sprays of n-dodecane fuel for these experiments. The injector was a solenoid-actuated unit from the set of Spray A injector of the Engine Combustion Network (ECN: https://ecn.sandia.gov/) [12]. Spray A specified injectors are equipped with 90-μm converging nozzle orifices (k-factor = 1.5). The sprays were injected at 150 MPa, with an electronic injection duration of 770 μs, producing 1.5-ms hydraulic injection duration, matching Spray A injection specifications. The sprays were injected into a constant-volume pre-burn combustion vessel able to simulate thermodynamic gas pressures and temperatures beyond typical engine conditions. The images are acquired from the top through a 100-mm diameter clear sapphire window. More information on the setup and installations is available in Ref. [10].

Further efforts have been made to minimize reflections to the imaging system, such as recessing the fused silica

window slits into the metal window ports, or the addition of internal non-reflective baffles to prevent back-reflections from the laser windows. The laser windows were also anti-reflection coated and cleaned repeatedly. In addition, most surfaces of the vessel were coated with high-temperature, high-absorption black paint or carbon-black electro-deposition process. Reflective elements that cannot be coated, such as spark-plug electrodes, were located not to produce interferences.

During these tests, the ambient conditions at the time of injection were kept constant and corresponded to the non-reacting Spray A case: 900 K temperature, 22.8 kg/m^3 density (60 bar) and 0% O2. This condition was chosen based on the success of Spray A within the experimental and modelling communities, but also because previous mixing measurements on this case [3] can be used for comparison. The thermodynamic conditions inside the vessel at the time of injection have been carefully characterized applying thin-wire thermocouple measurements, as well as Rayleigh scattering thermometry to evaluate the three-dimensional temperature distribution across the testing section.

RAYLEIGH SIGNAL QUANTIFICATION

The images were processed to extract quantitative mixing information following the method proposed by Espey et al. [7] for vaporizing jets in an optical diesel engine. The scheme was later applied to free high-pressure jets in the optical chamber used in the present experiments by Idicheria and coworkers [8] and Pickett et al. [3]. The high-speed aspect of the tests performed in this work require further corrections, such as dynamic spatial background corrections, in order to obtain time-resolved quantitative fuel concentration maps. Specific time-dependent correction methods were developed for these experiments, including routines correcting for two-dimensional background flare, contamination from particles, or spatial and temporal laser intensity variations. These methods, as well as the mathematics to obtain quantitative mixing information from the acquired Rayleigh signal were describe thoroughly in a recent publication [10]. The following paragraphs provide a brief description of these methods.

The first step of the image processing routine aims at correcting the high Rayleigh signal intensity scattered by contaminants, present in both the ambient or in the spray stream. Rayleigh scattering is dependent upon the cross-section of the illuminated particle, with a scattering intensity relationship following the sixth order on particle diameter [13]. Droplets are the most obvious source of larger scatterers in liquid injection studies, with penetrating droplets interfering with the Rayleigh scattered signal from the gaseous molecules. In the present study, the laser sheet was located far enough downstream to avoid liquid droplet scatter. Other sources of scatterers larger than the molecules include contaminants from the intake gases or the liquid fuel. Intake gases were filtered through a 3-nm in-line filter before entering the chamber. The n-dodecane fuel was of the highest available purity and was further filtered by cycling the fuel through a 100-nm membrane filter. Fuel pressurization was accomplished with a syringe pump to minimize moving parts and the fuel system volume. A 0.5-µm in-line filter was added to the high-pressure line feeding the fuel to the injector. These contaminants or particles have been a major issue across the different test campaigns on Rayleigh scattering when injecting liquid fuels. Previous attempts at correcting the images for particles applied spatial median filtering [8], but the large stencil degraded spatial resolution substantially. The use of image inpainting improved the process [14] by significantly reducing the size of the stencil area required to completely remove the interference from particles by spatial filtering. The automated process first evaluates the size of the largest particles contained in the image via binarization based on intensity distribution. Once the size distribution is known, the image is smoothed by a two-dimensional median filter. The median filter stencil size was determined from the particle size distribution to most effectively remove the particle interference. The algorithm compares the filtered and original image to identify the particle locations and spatial imaged dimension. Once particles are identified, a multi-pass image inpainting process [15] is applied to the region of each particle (or group of particles) to recover the particle-free signal intensity in this region. It is worth pointing out that only the regions contaminated by particles are affected by this process and that the rest of the image remains unaltered.

After the images have been corrected for particle contamination, the background flare is assessed and removed to obtain the Rayleigh signal intensity scattered by the ambient and fuel mixtures. Several parameters affect the intensity of the flare in the image background, such that each image needs to be individually corrected for background flare. In addition, it has been observed that the two-dimensional flare distribution must be adjusted on an image-by-image basis. The image-dependent two-dimensional flare is obtained by first assessing the background flare distribution with an empty vessel, to remove the Rayleigh scattered signal from the ambient gases. A control region outside of the laser sheet is selected to monitor the background flare intensity. An array of intensity-dependent background flare maps is created. Each acquired image is corrected by the appropriate background flare map according to the intensity measured in the control region. At this stage in the processing, all images are also corrected for camera system non-linearity, as detailed in Ref. [16].

The next step of the image treatment simultaneously corrects for spatial and temporal variations in laser intensity within the probed volume. Spatial variations in laser intensity in the chamber are mostly attributed to beam steering caused by temperature-induced density gradients at the window boundary. Some beam steering can also be induced by the temperature gradients within the spray. The different sources of beam steering are corrected by the method proposed by Gronki et al. [17]

and further developed by the authors [3, 8]. This method relies on the Rayleigh scattered signal in a uniform ambient gas such that the incoming and outgoing laser intensity profiles can be extracted from individual images. A linear interpolation is performed between both sides of the jet and mathematically compared to the original two-dimensional signal to correct the effect of beam steering and calibrate the signal simultaneously. This comparison process relies on the intensity ratio between the ambient gases and the fuel-ambient mixture. The intensity ratio between the fuel-ambient mixture and the ambient gases can then be used to assess the number density of fuel molecules within the jet. This approach offers many advantages, including self-calibration of the Rayleigh signal based on the comparison of signal from fuel molecules to that from the ambient gases of known composition and temperature. Use of the ambient signal for calibration eliminates the need for tedious characterization of the imaging system collection efficiency and simultaneously compensates for temporal and spatial laser intensity variations. The relationship between intensity ratio and molecular number density is given in Eq. 1:

$$\frac{I_{mix}}{I_{amb}} = \frac{\frac{\sigma_f}{\sigma_a}+\frac{N_a}{N_f}}{\frac{N_a}{N_f}+1} \cdot \frac{T_a}{T_{mix}}, \quad (1)$$

where I_{mix} and I_{amb} represent the intensity scattered by the mixture of fuel and ambient gases, and the intensity scattered by the ambient only, in that order. The Rayleigh cross-sections for the fuel and the ambient gases are labelled as σ_f and σ_a, respectively. Similarly, the molecular number densities are denoted by N_f and N_a, again for the fuel and ambient species. T_a is the temperature of the ambient gases and T_{mix} is the temperature of the fuel-ambient mixture. The temperature of the ambient and the mixture must also be known to extract fuel concentration (number density) information. The approach proposed by Espey et al. [7] assumes adiabatic mixing between the injected fluid and the ambient gases. This is a reasonable approach considering the relatively short duration of the event. We applied adiabatic mixing to relate the number density information to mixture temperature. The thermodynamic properties must be known over the range of temperature conditions (at the appropriate pressure point) to build an accurate relationship between number density ratio and mixture temperature. More information about the theory and mathematics to obtain quantitative mixing information is available in Ref. [14].

RESULTS AND DISCUSSIONS

The quantitative mixing fields and variance maps for the time-resolved experiments are presented and analyzed in this section. The mixing field and associated quantities are presented as mixture fraction Z, which was obtained from the number density of fuel and ambient molecules (c.f. Eq. 1) by the following relationships:

$$\frac{m_f}{m_a} = \frac{M_f}{M_a} \cdot \frac{N_f}{N_a}, \quad (2)$$

$$Z = \frac{m_f/m_a}{m_f/m_a + 1}. \quad (3)$$

In Eq. 2, m_f and m_a are respectively the mass of fuel and ambient at the measured location, and M_f and M_a are the molar masses for the fuel and ambient species, in that order.

Detailed mixing quantities such as two-dimensional scalar dissipation rates, as well as gradient thickness and orientation are also presented and discussed. As mentioned earlier, all the experimental results reported in this work correspond to the Engine Combustion Network Spray A condition.

Figure 2 presents a panel of two-dimensional mixture fraction fields acquired at different timings showing the spray development and mixture distribution for Spray A. As a reminder, the ambient temperature and pressure conditions for Spray A are 900 K and 6.0 MPa, respectively, with a fuel injection pressure of 150 MPa and a 1.5-ms injection duration. The image panels in Fig. 2, as well as other two-dimensional mixing results presented thereafter, show the region of the jet from approximately 15 to 35 mm downstream of the injector outlet. The maps are displayed in false color to highlight the broad fuel concentrations observed in high-pressure diesel jets.

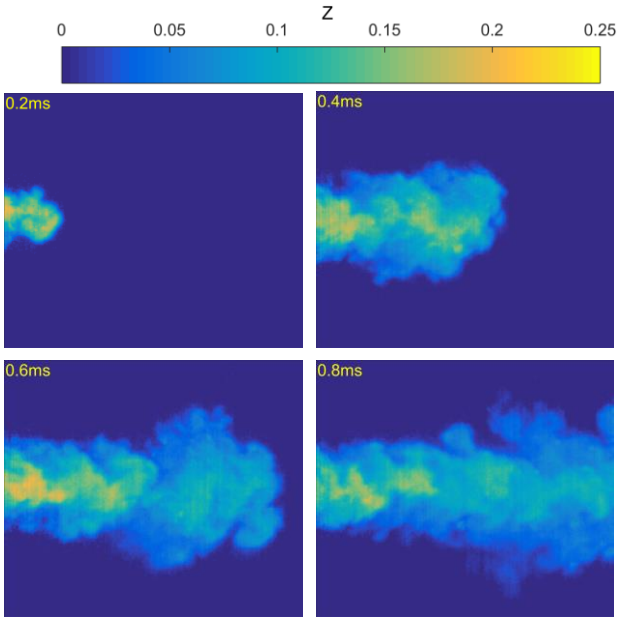

Fig. 2 Sample mixture fraction fields extracted from a single event at different timings during injection. The time label at top left is given with respect to the start of injection. The maps cover the axial distance from approximately 15 to 35 mm from the injector exit.

The mixture fraction evolution of Fig. 2 highlights the turbulent aspect of the flow that remains even at these long distances (200 diameters and beyond) into the far-field. Probing a region relatively far from the injector exit limits the measured mixture fraction quantities to approximately Z = 0.25 and lower. The spatial variation in mixture fraction can be appreciated from these instantaneous shots,

with generally richer mixtures near the jet centerline, and leaner mixtures on the periphery. These images show that high mixture fraction pockets can be observed on the periphery and conversely, some lean regions can be seen near the jet axis. The different timings of the sequence show large-scale structures being pushed to the side of the jet and re-entrained into the jet stream behind the spray head at later timings. It is interesting to observe the lower and more uniform mixture fractions measured in the head of the jet at later timings during the event. The last timing of the sequence offers a global perspective on the mixing field in this region, showing that mixture fraction generally decreases for locations farther from the injector.

The average mixing field is calculated by averaging the several repetitions to generate ensemble-average maps at different timings. Figure 3 presents the ensemble-average mixture fraction fields at the same timings shown in Fig. 2. These average mixture fraction maps were obtained by averaging the synchronized mixing fields from the different injection repetitions available at selected timings after the start of injection.

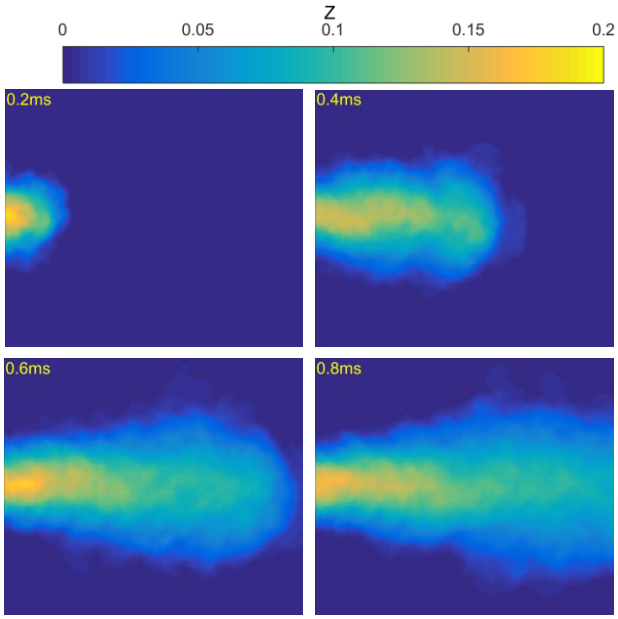

Fig. 3 Ensemble-averaged mixture fraction fields at different timings during injection from 10 injections. The mixture fraction maps have been averaged over several repetitions. The time label at top left is given with respect to the start of injection.

As expected, the ensemble-averaged mixture fraction fields are substantially smoother such that the smaller and sharper detailed features are no longer observed as they were in the single event results shown in Fig. 2. The steep gradients and wide range of mixture fractions scattered in the jet stream for a single injection event are replaced by continuous transitions. The time evolution of the jet head is interesting as it initially presents high mean mixture fractions, but gets leaner at later timings. The earlier comment about lower mixture fractions with axial distance is clear at late timings of Fig. 3, after the head of the jet has exited the visualized region. These images offer a perspective on the quasi-steady mixing field over the probed region. It can nevertheless be appreciated that the limited number of repetitions available (10) to generate time-resolved ensemble-averaged maps produce mixing fields lacking convergence. This is particularly noticeable in the jet periphery, while the central regions appear smoother and more continuous. The turbulent nature of high-speed jets produces high spatial and temporal variations in mixture fraction. A large part of the uncertainty in quantifying the average mixture fraction under these conditions comes from the limited number of injections. For fundamental analysis of the uncertainty of the mixture fraction measurements, we refer the reader to Ref. [14].

The variability of the jet provides a measure of the mixing fluctuations and can be visually assessed by representing the mixture fraction variance or standard deviation computed over time, or across injection repetitions. The variability at a particular instant in time can be estimated by computing the standard deviation for the ten injections available. The jackknife resampling method [18] has been used to enhanced the statistical validity of the turbulent-induced mixing variability. The standard deviation has been calculated from the spatially filtered images used to compute the average mixture fraction maps shown in Fig. 3. The standard deviation maps shown in Fig. 4 are also reported at different timings during the injection event.

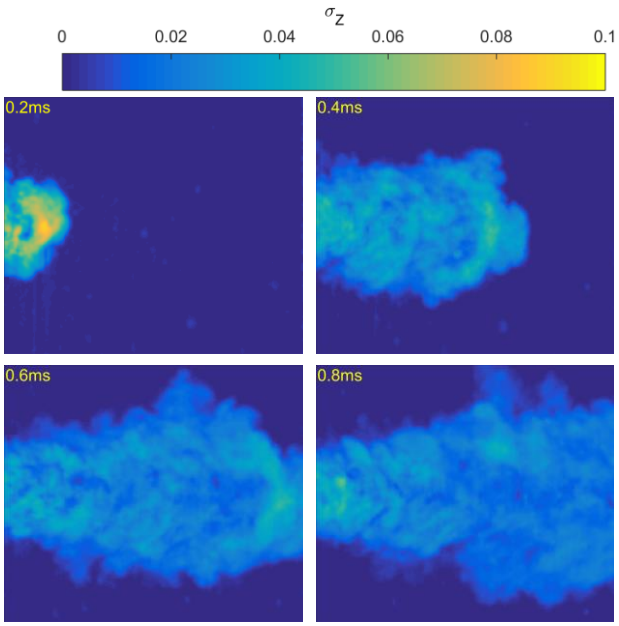

Fig. 4 Standard deviation of the mean mixture fraction field across injection repetitions at different timings during injection enhanced via Jackknife resampling. The time label at top left is given with respect to the start of injection.

The standard deviation across injection repetitions at various timings show a fair amount of variability, with standard deviation magnitudes of approximately half the mean mixture fraction. This variability is a combination of the injection repeatability, as well as fuel-ambient mixing turbulence. The variability is particularly high at

earlier timings, where injection-to-injection jet development produces standard deviation quantities over half the mean mixture fraction (c.f. Fig. 3). Again, the limited number of repetitions does not produce well converged variability results, even though the convergence has been improved by the Jackknife resampling method.

The rate of mixing at the molecular level in turbulent single-phase systems is commonly characterized by the scalar dissipation rate. The scalar dissipation rate χ is a measure of the rate of molecular mixing, and is defined as:

$$\chi = 2D.|\nabla Z|^2. \quad (4)$$

The mass diffusivity D would fluctuate across the mixing field due mainly to temperature variations. Considering the adiabatic mixing temperature in the investigated region, the mixture temperature would drop from 900 K in the ambient to about 600 K for the rich mixtures measured upstream. Applying the correlation proposed by Erkey et al. [19], the mass diffusivity between the fuel (n-dodecane) and N_2 would vary from approximately 0.25 to 0.53 mm^2/s for the aforementioned temperature range. As suggested by Kaiser and Frank [11], the mass diffusivity can be omitted if the objective is to investigate mixing gradient thickness and orientation, due to the relative nature of these measurements. Thus, the results presented hereafter consider only the squared gradient of the mixture fraction field ($|\nabla Z|^2$), as opposed to the scalar dissipation rate quantities. Figure 5 shows individual maps of $|\nabla Z|^2$ acquired at different timings after the start of injection. These maps of $|\nabla Z|^2$ correspond to the mixture fraction fields shown in Fig. 2, with a 3-by-3 pixels spatial Gaussian filtering.

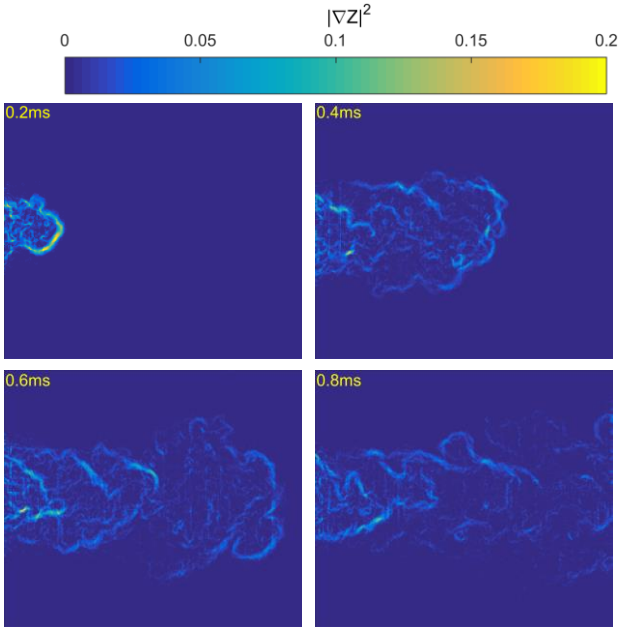

Fig. 5 Squared gradient of the mixture fraction taken at different timings during injection on a single event. The maps show the dissipative structures in space and time during the event. The time label at top left is given with respect to the start of injection.

The $|\nabla Z|^2$ maps of Fig. 5 show the evolution of the jet and mixing structures as the jet develops and mixes with the ambient gases. The gradient maps highlight the contour definition of the large-scale structures, rather than the smaller scales. It can be appreciated that the magnitude of $|\nabla Z|^2$ is higher in the jet head, with maxima upward of 0.2 mm^2. We can also observe that the magnitude of $|\nabla Z|^2$ generally decreases with axial distance. This reduction is expected because the mixture gets leaner at farther downstream locations, as shown in Fig. 2. In addition, the lower velocities found in downstream locations have reduced shear, thus contributing to lower mixture gradients. Even after the Gaussian filtering has been applied to the fields, gradients induced by beam steering and shot noise are still visible. Higher filtering levels would certainly reduce these effects, but also affect the magnitude of the gradients. The uncertainty regarding gradient quantification produced by the actual optical performance of the imaging system in terms of spatial resolution will be evaluated later in this manuscript.

Information about the magnitude of $|\nabla Z|^2$ and its thickness can be extracted from the various two-dimensional maps of $|\nabla Z|^2$ for the mixing field. Previous studies in reacting and non-reacting flows [11, 20] evaluated the turbulent length scales by measuring the magnitude of the dissipative structures on the squared gradient mixing and their widths at a 20% threshold. Consistent with these aforementioned studies, the procedure carried out in this work first finds the centerline or peak of the gradient and then measures the width or thickness of the layer perpendicular to the gradient profile. In many instances, the dissipative structures are close to one another requiring that the half-widths at a 20% gradient level be measured separately and then doubled to improve the number of quantified layer thicknesses. It is important to note that the artificial gradients produced by shot noise and beam steering are well below the detection threshold of the gradient quantification procedure.

The magnitude of the gradients or steepness of the mixing contours in the high-pressure diesel jets tested in this study were statistically evaluated by gathering the values of the gradient maxima over the quasi-steady period of the injection. The peak values of the squared gradient measured from 17 to 35 mm downstream of the nozzle exit are reported in the distribution plotted in Fig. 6. These statistics combine the measured gradients on the images recorded from approximately 0.7 ms after the start of injection until the end of injection for the various repetitions available. It must be noted that only the top 90 % of the squared-gradient maps have been considered to avoid artificial gradients induced by the beam steering to affect the statistics.

The distribution of squared gradient peaks reported in Fig. 6 indicates that most of the dissipative structures are smooth, with a distribution average value slightly above 0.04 mm^2. Assuming the mass diffusivity range mentioned above, such squared gradient quantities would equate to scalar dissipation rates on the order of 0.02 s^{-1} in fuel-lean

regions where temperatures are close to the ambient. Richer mixtures are generally characterized by steeper gradients, but also lower temperatures, leading to higher scalar dissipation rates—but still well below 0.1 s^{-1} as expected. These quantities may seem low compared to those reported for turbulent gas jets [21], but recall that this analysis is performed at distances near and beyond 200 outlet diameters downstream of the injector outlet. In addition, the high pressures in the environment (6.0 MPa) result in substantially lower diffusion coefficients, thus bringing the scalar dissipation rates down.

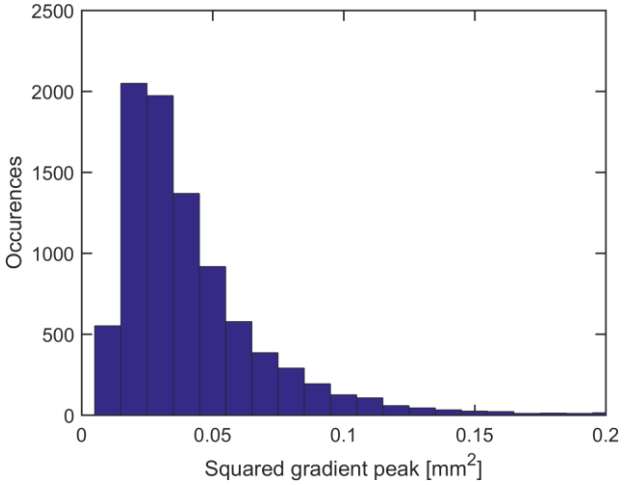

Fig. 6 Distribution of squared-gradient maxima of the mixture fraction during the quasi-steady period of the injection. The gradients were quantified on several injections in the region between 17 and 35 mm downstream of the injector.

The thickness of the gradient is important as it indicates the spatial spread of the dissipative structures from rich mixtures to lean regions and vice versa. As described earlier, the thickness of the mixing layers was evaluated on the squared gradient maps at 20 % of the peak. The dissipative structure widths reported in the distribution of Fig. 7 were measured simultaneously to the gradient peaks of Fig. 6. As such, gradients lower than 10 % of the peak gradients were not considered.

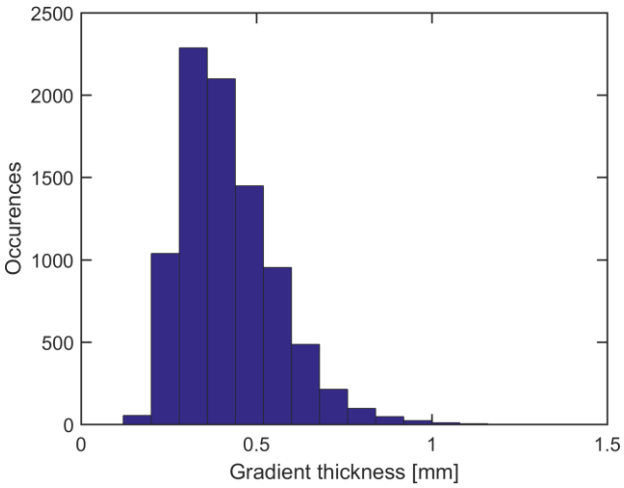

Fig. 7 Distribution of mixture gradient thickness at 20 % threshold over the quasi-steady period of the injection and multiple events.

The gradient thickness is characterized by a relatively narrow distribution, contained between approximately 0.2 to 1.0 mm. It must be reminded that according to the resolution measurements reported earlier in this manuscript, scales on the order of 0.2 mm represent the measurement limit at these conditions. The average gradient thickness was measured at 0.42 mm. The peak of the distribution resembling a log-normal is located between 0.3 and 0.4 mm in width. These gradient thickness quantities are comparable to length scales measured in turbulent flames and gas jets [22, 23]. These measurements were in general performed at atmospheric conditions. The high ambient temperatures and pressures of the present experiments are likely to affect the mixing substantially. It can be noted that ambient pressure is expected to produce steeper gradients. On the other hand, measurements by Frank and Kaiser [23] suggest that high ambient temperatures broaden the dissipative layers. The lack of comparable data for diesel jets at any condition highlights the importance and uniqueness of the present results and analysis.

At the same time, the uncertainty associated with the dissipative structures must be carefully quantified. Beyond the limited number of repetitions to obtain statistically converged mixing fields, the uncertainty on mixture quantities mainly comes from boundary conditions and error in estimating the Rayleigh cross section of the molecules at the experimental conditions. This error was evaluated in previous works [3, 14], and was estimated at around 2.5 %. The higher uncertainty in the dynamic flare correction procedure due to the high-speed nature of the present experiments certainly contributes to higher mixture fraction uncertainties. However, the error on layer thickness would be immeasurable, while similar error to the mixture fraction would be replicated onto squared gradient maxima. Because of the sub-millimetric measured scales, the resolution of the imaging system is paramount to quantifying detailed mixing structures. The uncertainty in gradient quantification can be evaluated as it relates to the image resolution tests reported earlier in this manuscript. Wang and Clemens [24] numerically evaluated the impact of imaging resolution on the quantification of mixing structures, including peak gradient, peak dissipation rate and dissipative layer thickness. The authors based their analysis of the associated error on the response of the imaging system, assuming a Gaussian-shaped line spread function. The Gaussian-like profile reported in Fig. 1 confirms that this approach is appropriate. The error can be estimated from the measured width of the line spread function. The standard deviation of the Gaussian distribution that best matches the measured line spread function is used to estimate measurement error. The best fit to the measured line spread function was achieved with a Gaussian distribution of 78-µm standard deviation. Following the analysis undertaken by the authors to evaluate the error associated with the measured spatial

resolution of the imaging system reveals an error below 10 % for the gradient peak and just above 10 % for the gradient thickness for the mean layer width (0.42 mm). These figures would increase to 27 and 37 %, respectively, when measuring gradients on the order of 0.2 mm, corresponding to the smallest resolved scales. The error would decrease to approximately 2 % for layer width around 1 mm. The relatively large error committed on the smaller layer widths can be expected to bias the distribution of Figs. 6 and 7 toward slightly smaller scales. Overall, both the squared gradient peak and thickness average values should be about 10 % higher than the measurements returned.

The orientation of the gradient is another important parameter of mixing, especially in turbulent non-premixed combustion. In jet-induced mixing, gradient orientation is driven by the velocity difference between the injected flow and the relatively stagnant ambient. The shear generated at the mixing layer orients the gradient according to various parameters such as velocity and density differences between the mixing fluids. The mixing gradient orientation has been extracted simultaneously with the gradient peak and thickness from the squared gradient maps. The orientation of the gradients is represented by the angle between the jet axis and the profile following the gradient peaks. The distribution of the gradient angle for the region between 17 and 35 mm downstream of the injector exit is reported in Fig. 8. The axial direction or the jet axis corresponds to the 0-degree dashed line position. Dashed lines at -90 and 90 deg. indicate gradient angles orthogonal to the jet axis.

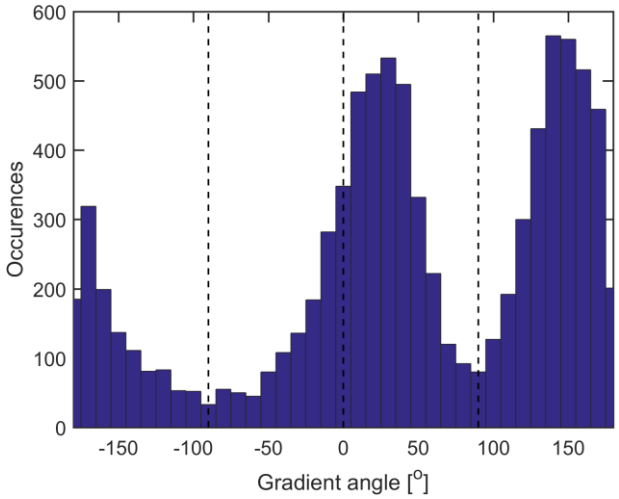

Fig. 8 Distribution of mixture gradient orientation (angle) during the quasi-steady period of the injection for several repetitions.

The gradient orientation distribution of Fig. 8 shows a mainly bi-modal distribution peaking at approximately 30 and 150 degrees. The smaller peak centered at -90 degrees is a manifestation of the effects of beam steering, as mentioned above. The angle considers the actual orientation of the gradient, carrying information on the direction of the gradient, from rich to lean mixtures or vice versa. The 30-deg. angle represents the gradients on the upper half of the maps shown in Fig. 7, from richer to leaner mixture while moving away from the jet axis. The 150-deg. position is the symmetrical orientation, corresponding to the lower half of the jet, from higher to lower mixture fractions when moving away from the jet centerline. These results show that mixing occurs along a preferred angle near 30 degrees from the jet axis, on both sides. The narrower 30-degree angle observed in this work relative to a mixing layer orientation centered around 45 deg. for turbulent gas jets may be explained by flow velocities and density differences. The near sonic velocities combined with the higher molar density of the fuel [25] lead to higher momentum in the jet stream. This higher momentum could contribute to the narrow mixing field of diesel jets when compared to atmospheric gas jets. More investigations are necessary to identify other potential reasons for the narrower orientation of the mixing gradients measured in these high-pressure diesel jets. The error related to imaging system resolution on gradient orientation is believed to be limited and should not impact the main conclusions drawn from the analysis of the results detailed above. In addition, it can be noted that, similarly to the gradient thickness, uncertainty in mixture fraction would have no measurable effect on dissipative structure orientation.

CONCLUSIONS

Time-resolved quantitative measurements of evaporative diesel jet mixing processes have been performed in an optically accessible chamber at engine relevant operating conditions. Planar laser Rayleigh scattering was implemented at high-speed to fully resolve the spatial and temporal evolution of the vaporized region of the jet.. To achieve the illumination energy requirement to measure Rayleigh signal at high-speed, a 100-kHz high-power pulsed burst laser was developed and built. A state-of-the-art commercial high-speed camera was equipped with optimized optics to maximize collection efficiency and spatial resolution in order to record the Rayleigh signal from the ambient gases and fuel molecules. Advanced image processing methodologies were implemented to mitigate the effects of particle contamination, laser intensity variation and jet-induced beam steering. An adaptive flare correction method, responding to both spatial and temporal variations has been developed to correct the images and quantitatively assess fuel mixtures in time and space.

The temporally-resolved mixing fields at various timings were analyzed to show the average mixture distribution during jet development as well as the variability between repetitions. As expected, the mean mixture fraction field shows richer mixtures in upstream regions, but somewhat inconsistent with instantaneous shots, the head of the jet did not show particularly higher mixture fractions. Variability was strongly correlated with the state of mixing, with higher variability in upstream regions. Regions near the periphery of the jet showed high variability compared to the mean, as expected, because of shot-to-shot variability in jet development between injections. The variability between injections was

compared to the temporal standard deviation over the quasi-steady period of the injection, showing the higher variability between injection repetitions. Detailed mixing quantities were investigated by analyzing the scalar dissipation rate via the squared gradient of the mixture fraction at various timings. We observed that gradients were steeper in upstream regions, again related to the richer mixtures. Dissipative structure peaks, widths and orientations were extracted from the squared gradient fields over the quasi-steady period of multiple injections. Squared gradient peaks were observed to be relatively small, with a mean peak distribution below 0.04 mm^2. The small value is due to the analysis being carried out in the far-field region of the jet. Gradient thickness was comparable to widths measured in turbulent gas jets, with a distribution average close to 0.4-mm wide across the investigated region. The gradient angle distribution showed that the mixing layer was oriented at approximately 30 degrees from the jet axis on average, with dominantly rich mixtures near the jet centerline. The narrowness of the mixing layer orientation relative to gas jets suggests that the high flow velocities in diesel jets, combined with the higher fuel molar density strongly affect mixing. These detailed mixing quantities need to be investigated further via high-resolution planar laser Rayleigh scattering imaging to confirm the findings of this work.

Acknowledgements
The authors thank Dr. Bruno Coriton (General Atomics) for the discussions on mixing statistics and for sharing the processing methods about layer thickness. This study was performed at the Combustion Research Facility, Sandia National Laboratories is a multi-mission laboratory managed and operated by National Technology and Engineering Solutions of Sandia, LLC., a wholly owned subsidiary of Honeywell International, Inc., for the U.S. Department of Energy's National Nuclear Security Administration under contract DE-NA0003525.

REFERENCES

[1] H. Zhao and N. Ladommatos. *Prog. Energ. Combust.*, 24(4):297–336, 1998.
[2] J. Egermann, A. Gottler, and A. Leipertz. *SAE 2001-01-3496*, 2001.
[3] L. M. Pickett, J. Manin, C. L. Genzale, D. L. Siebers, M. P. B. Musculus, and C. A. Idicheria. *SAE Paper 2011-01-0686 - SAE Int. J. Engines*, 4(1):764–799, 2011.
[4] T. D. Fansler, M. C. Drake, B. Gajdeczko, I. Duwel, W. Koban, F. P Zimmermann, and C. Schulz. *Measurement Science and Technology*, 20(12):125401, 2009.
[5] Y.-Y. Zhang, T. Yoshizaki, and K. Nishida. *Appl. Optics*, 39(33):6221–6229, 2000.
[6] V. Sick. *Proc. Combust. Inst.*, 34(2):3509–3530, 2013.
[7] C. Espey, J. E. Dec, T. A. Litzinger, and D. A. Santavicca. *Combustion and Flame*, 109(1-2):65–78, 1997.
[8] C. A. Idicheria and L. M. Pickett. *SAE Paper 2007-01-0647*, 2007.
[9] A. Adam, P. Leick, G. Bittlinger, and C. Schulz. *Exp. Fluids*, 47(3):439–449, 2009.
[10] J. Manin, L. M. Pickett, S. A. Skeen, J. H. Frank, Patterson B., and S. E. Bisson. *ILASS-Europe 2016, Brighton, UK*, 2016.
[11] S. A. Kaiser and J. H. Frank*Proc. Combust. Inst.*, 31(1):1515–1523, 2007.
[12] L. M. Pickett, C. L. Genzale, G. Bruneaux, L.-M. Malbec, L. Hermant, C. Christiansen, and J. Schramm. *SAE Int. J. Engines*, 3(2):156–181, 2010.
[13] J.W. Strutt Rayleigh. *Philos. Mag.*, 41(271):107–120, 1871.
[14] Julien Manin. PhD thesis, CMT - Motores Termicos. Universidad Politécnica de Valencia, Spain, 2011.
[15] D.J. Heeger and J.R. Bergen. *Proceedings of the 22nd annual conference on Computer graphics and interactive techniques*, pages 229–238, 1995.
[16] J. Manin, L. M. Pickett, and S. A. Skeen. *ILASS-Americas 2016, Dearborn, MI*, 2016.
[17] J. Gronki, C. Schulz, and H. Scharr. *Eurotherm Seminar 2002, Visualisation, Imaging and Data Analvsis in Convective Heat and Mass Transfer*, pages 301–306, 2002.
[18] L. H. Benedict and R. D. Gould. *Experiments in fluids*, 22(2):129–136, 1996.
[19] C. Erkey, J. B. Rodden, and A. Akgerman. *The Canadian journal of chemical engineering*, 68(4):661–665, 1990.
[20] L. K. Su and N. T. Clemens. *Journal of Fluid Mechanics*, 488:1–29, 2003.
[21] J. H. Frank and S. A. Kaiser. *Experiments in fluids*, 49(4):823–837, 2010.
[22] M. Tsurikov and N. Clemens. *40th AIAA Aerospace Sciences Meeting & Exhibit*, (164), 2002.
[23] J. H. Frank and S. A. Kaiser. *Experiments in Fluids*, 44(2):221–233, 2008.
[24] G. H. Wang and N. T. Clemens. *Experiments in fluids*, 37(2):194–205, 2004.
[25] R. N. Dahms, J. Manin, L. M. Pickett, and J. C. Oefelein. *Proceedings of the Combustion Institute*, 34(1):1667–1675, 2013.